JOURNAL OF THEORETICAL
AND APPLIED MECHANICS
63, 3, pp. 535–543, Warsaw 2025
https://doi.org/10.15632/jtam-pl/202686

RESPONSE OF SANDWICH STRUCTURES WITH NOVEL TPMS CORES UNDER CYCLIC UNIAXIAL COMPRESSION

Alexandru VASILE[1,2*], Iulian Constantin COROPEŢCHI[1,2], Andrei Ioan INDREŞ[1],
Dan Mihai CONSTANTINESCU[2,3], Ştefan SOROHAN[2], Dragoş Alexandru APOSTOL[2]

[1] *Faculty of Aircraft and Military Vehicles, Military Technical Academy "Ferdinand I", Bucharest, Romania*
[2] *Department of Strength of Materials, National University for Science and Technology POLITEHNICA Bucharest, Bucharest, Romania*
[3] *Institute of Solid Mechanics of the Romanian Academy, Bucharest, Romania*
*corresponding author, *alexandru.vasile@mta.ro*

This paper focuses on the compressive behavior of nine triply periodic minimal surface (TPMS) structures and one stochastic geometry, designed through an implicit modeling approach and fabricated using a stereolithography (SLA) technique. The compressive response is analyzed, with two topologies outperforming the well-known gyroid, in terms of rigidity and yield strength. Low cyclic testing at two strain levels highlights the good repeatability and stability of the proposed topologies, while comparing the specimens from an energy absorption performance and residual deformation perspective. The stochastic geometry exhibited the worst recovery rates, even though it had the second-best energy absorption capabilities for the single compression testing.

Keywords: TPMS; implicit modeling; sandwich structures; cyclic compression.

1. Introduction

Current literature provides many valuable observations regarding general mechanical properties, failure modes and possible applications of sandwich structures with metamaterial cores. From constant cross-sectional structures such as honeycombs or chiral topologies, to complex three-dimensional geometries such as cores based on interconnected ligaments, foams or foldable walls, all have been extensively studied and implemented in practical applications. However, with the advancements in additive manufacturing technologies, very complex topologies can now be generated and analyzed with methods involving an automated approach. A more detailed classification of existing types of sandwich structures with metamaterial cores is presented in (Feng *et al.*, 2020; Lu *et al.*, 2022; Yu *et al.*, 2018).

Recent studies have shown a growing interest in exploring thin-walled structures based on TPMS, particularly those produced using additive manufacturing techniques. Findings suggest that these structures outperform traditional topologies in terms of rigidity, compressive strength, energy absorption capabilities and mechanical behavior predictability (Al-Ketan *et al.*, 2019; Araya *et al.*, 2024). These characteristics make TPMS-based geometries particularly appealing for advanced engineering applications, including aerospace, automotive, and biomedical fields (Cresswell *et al.*, 2024; Gabrieli *et al.*, 2024). Their mathematically defined periodicity allows

---

Ministry of Science and Higher Education
Republic of Poland

The publication has been funded by the Polish Ministry of Science and Higher Education under the Excellent Science II programme "Support for scientific conferences".
The content of this article was presented during the 40th Danubia-Adria Symposium on Advances in Experimental Mechanics, Gdańsk, Poland, September 24–27, 2024.

for precise tailoring of mechanical properties, while advancements in additive manufacturing technologies have facilitated the fabrication of these complex geometries, opening new possibilities for optimizing material efficiency and structural resilience. Understanding and further developing TPMS structures is, therefore, critical for advancing next-generation materials and structural solutions.

Comprehensive investigations into the mechanical properties of commonly used TPMS structures, as highlighted by Gao *et al.* (2024), Ronca *et al.* (2019), Wei *et al.* (2024), Yang *et al.* (2023), offer valuable insights into the different domains where such topologies can be used. Adjusting the dimensions and orientation of the representative cell or employing a gradient-based design approach are methods for customizing the mechanical response of TPMS structures, including their energy absorption capacity and overall stability. Key articles that provide insights into how modifications to the fundamental geometry influence the mechanical properties include: Novak *et al.* (2022), Ramírez *et al.* (2024), Song *et al.* (2024), Viet *et al.* (2023).

Research on TPMS structures has largely focused on analyzing the properties and performance of predefined geometries, with little interest directed towards developing new types of topologies. Thus, this paper aims to present the compression behavior of sandwich structures with novel metamaterial cores, while understanding their mechanical properties, deformation mechanisms and energy absorption capabilities through low cyclic compressive testing.

2. Sample definition and fabrication

This study focuses on analyzing the behavior of ten types of sandwich structures. The first sample, the well-known gyroid, described initially by Schoen (1970), serves as a benchmark topology frequently encountered in relevant literature. Alongside it, nine additional geometries were proposed. The first eight are novel TPMS type topologies, based on continuous, self-supporting and non-intersecting surfaces. These are described by the equations presented by Vasile *et al.* (2024). The formulas are heuristically determined in order to obtain structures that do not need internal supports, allowing for scalability of the topology and avoiding the generation of enclosed chambers, which would be filled with resin or powder during the manufacturing process and modify the final characteristics of the geometry. At the same time, the functions were chosen in order to cover a broad range of topology types, that are currently being researched: bi-cameral geometries (S1, S3, S8), re-entrant type 3D structures (S2), designs with wall thickness gradient (S5), small feature topologies (S6), lattice 3D arrangements (S7), geometries with layers at an angle (S4, S9), foam-like structures (S10). Sample 10 is stochastically determined, with struts conditioned to align with the z-direction, defined as perpendicular to the two sandwich sheets, with an average distance between the ligaments of 3.5 mm and with an average number of ligaments intersecting at the same point being 6.

All the topologies were generated through an implicit approach method, using the *nTopology software* to generate thin-shelled cells. Each representative volume element was defined as a cube with 10 mm sides, which was multiplied to generate the metamaterial core. It incorporated $3 \times 3 \times 3$ such unit cells, to form a cube with 30 mm sides, which was placed between two 3 mm sheets as to obtain the final sandwich geometry. The cell wall thickness was adjusted to maintain a constant relative density of 0.3 across all the proposed samples.

All specimens were fabricated from the same material, in the form of a photosensitive polymer resin, Tough 1500v1, using a Formlabs Form L stereolithography printer, with a layer thickness of 50 μm. The post-cured average mechanical properties established by us through tensile testing are: ultimate tensile strength – 34.47 MPa, tensile Young's modulus – 1.29 GPa, and elongation at break – 26 %. Post-processing of the samples was performed using an automated washing and curing station. Details on the fabrication technique and geometry analysis of the samples are presented in (Vasile *et al.*, 2024). Figure 1 displays the printed samples after post-processing and removal of lateral supports.

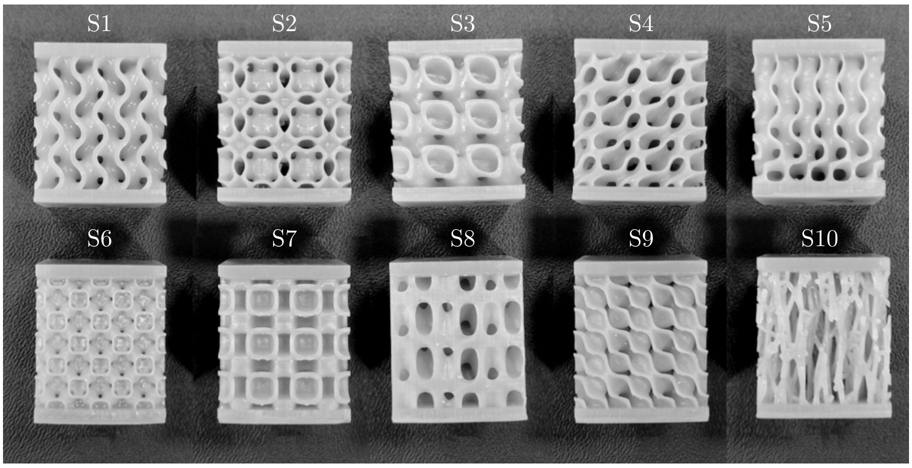

Fig. 1. Ten topologies of printed samples.

3. Low cyclic compression testing

First, quasi-static uniaxial compression tests were carried out on the architected samples, according to the ASTM D695 standard. Figure 2a highlights the compressive force as a function of deformation for the proposed structures. The tests are presented in detail in (Vasile *et al.*, 2024).

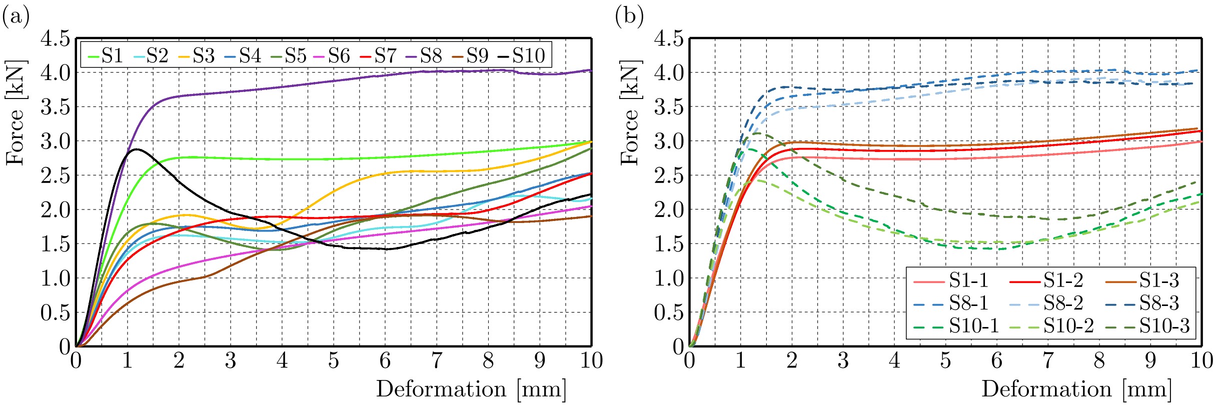

Fig. 2. (a) Variation of compressive force as a function of deformation for the proposed structures; (b) compressive force as a function of deformation for three tests carried out under identical conditions for S1, S8 and S10.

While most samples provided a similar response in terms of loading force, S1, S8 and S10 stand out as outliers. S10 the stochastic structure, proved to be the geometry with the greatest stiffness, exhibiting a higher yield force than the gyroid, but presenting an intense softening effect in the plastic region, due to fracture of the struts. This, in turn, greatly affects the energy absorption capabilities of the structure. Topology S8 exhibited a similar behavior to the gyroid, with values corresponding to the yield point up to 31 % higher than the gyroid counterpart. However, unlike the gyroid, it exhibited internal cracks at high deformations of approximately 23 % strain. These were observed in the outer surfaces of the specimen, but did not lead to premature generalized failure and are a result of the generated thin walls when confining the topology to a 30 mm cube domain.

In order to validate the repeatability of the results obtained experimentally, subsequent tests were carried out on the same type of specimens. Both the manufacturing and testing methods were maintained constant. Figure 2b shows the plots of the loading force versus the deformation for three tests for three of the proposed topologies. A similar behavior is observed in the elastic region, with limited variation in the plastic zone, the largest deviations occurring for the stochastic sample (S10), where the nature of the geometry generates lower repeatability. During S8 testing, the same fractures of the outer walls were visible. However, during the three tests, a maximum positive variation of up to 9 % in the force corresponding to yielding was observed, compared to the gyroid (S1) which had a maximum variation of only 7 %. This variation was attributed to insufficiently rigorous control following the printing procedure and during the sample washing and treatment processes.

Cyclic uniaxial compression tests were performed to evaluate the energy absorption capacity and recoverability of the proposed samples. Two complementary scenarios of loading and unloading cycles were considered, using the same testing set-up, at a speed of 1 mm/min.

In order to capture the behavior in the elastic region, the first scenario tested the samples for 100 cycles, up to a deformation of 0.15 mm (0.5 % strain) from the initial undeformed configuration. After the testing was concluded, another cycle was conducted after one hour, in order to study the recoverability of the specimens.

Figure 3a displays the compressive force as a function of deformation, for all 10 samples, for the 1st (C1), the 100th (C100), and the 101st (C101) cycles of loading-unloading. This additional cycle was captured, as already mentioned, one hour after the first 100 were finished, in order to observe the recovery rate of the specimens. The scale has been maintained constant in order to facilitate easier comparison between the samples. It can be seen that the evolutions are in accordance with the results shown in Fig. 2a, with the unloading curves following a different path, leading to hysteresis loops. These loops illustrate energy dissipation within the material, caused by internal mechanisms such as atomic rearrangements and nonlinear effects. Also, all the samples show a residual strain at the end of the cycle, which is due to the fact that the recovery rate is lower than the 1 mm/min speed used for tensile testing. The S10 stochastic structure shows the highest hysteresis loop area during the first cycle, pointing to a better energy absorption capability, while the structure S8 displays the highest stiffness.

It is noticeable that even though the loops continuously move towards lower values for loading force and higher residual strain, the behavior is stable, with both the loading and unloading cycles following similar patterns. The red curves which capture the additional cycle, overlap the first cycle in almost all the specimens, showing that all the TPMS have good recovery capabilities. An offset is visible in the case of S10, which means that the geometry did not fully return to the initial dimensions during the one-hour interval considered for recovery. This proves that the TPMS geometries exhibit better elastic recovery than the stochastic one, when subsequent tests are performed.

When comparing the residual deformation during the first 100 cycles, as shown in Fig. 3b, S8 proves to be the stiffest, with the lowest values of residual deformation, while S9 ranks first and the gyroid occupies the 4th position. This highlights how fast the force-deformation loops decrease in value, with S8 maintaining higher performance over a greater number of cycles.

Figure 3c shows the total amount of energy absorbed during loading for all the 100 cycles, along with the quantity of this energy that is dissipated through the hysteresis. On average, the hysteresis accounts for approximately 22 % of the loading energy, with S8 being an outlier, as only 18 % of its energy is dissipated internally due to its lower residual deformation values. It can be noticed that the stochastic topology S10 outranks the gyroid S1 in terms of energy absorption. Additionally, as an interesting observation, the S5 topology, which was designed with a wall thickness gradient along the axis of deformation (thickness being increased towards the bottom of the specimen), demonstrates very good energy absorption capabilities compared to the other specimens tested.

Figure 4a displays the energy absorption capabilities for the specimens during the 100 cycles considered. While all the samples show a descending trend, toward a value where the damage behavior stabilizes, it is clear that S10 (light-grey curve) has a slightly higher descending slope during the first cycles. The values are also in accordance with the variations displayed in Fig. 2a.

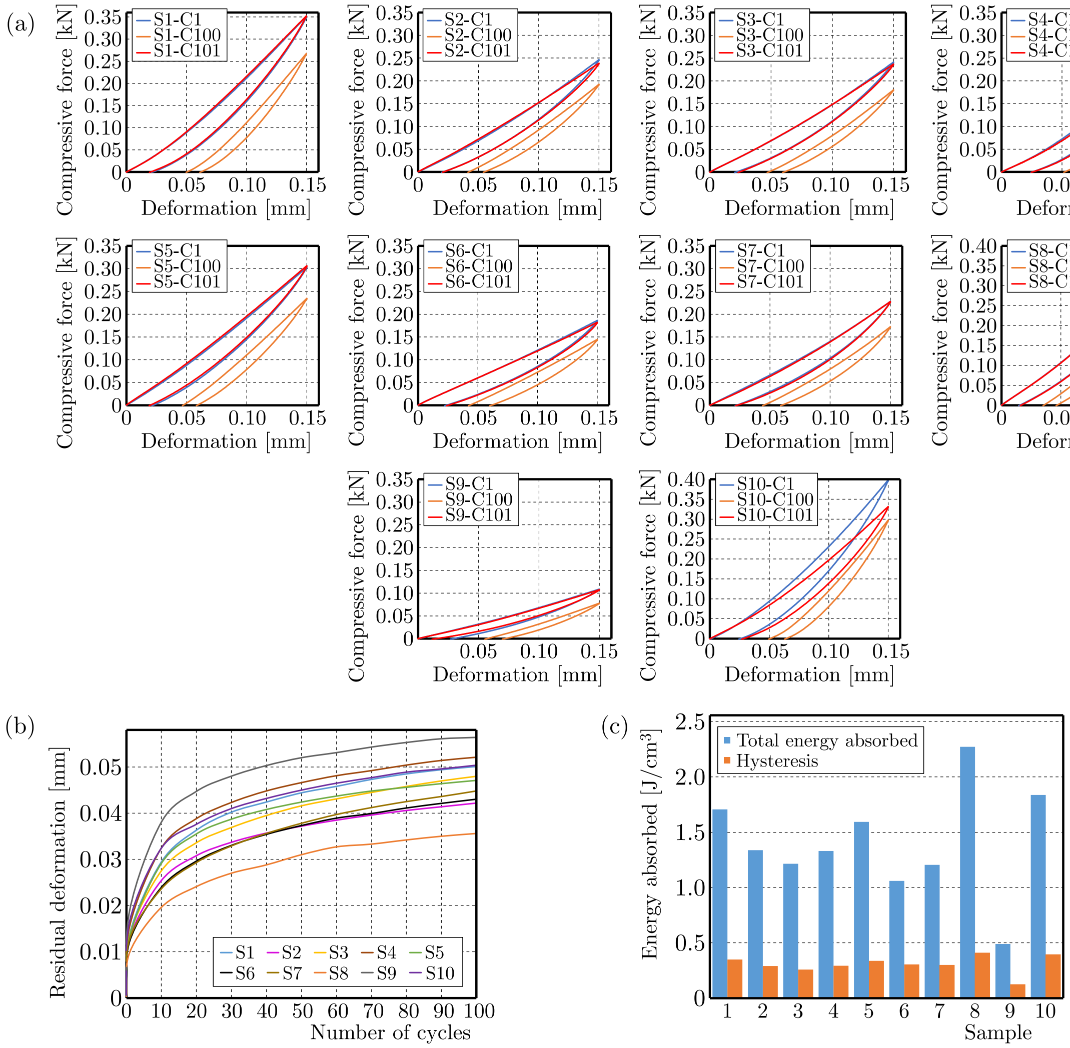

Fig. 3. (a) Cyclic compression results showing compressive force vs deformation plots for the 1st cycle (blue), the 100th cycle (orange) and an additional cycle after one hour of recovery time (red) for all topologies; (b) residual deformation accumulation during 100 cycles; (c) total energy absorbed and hysteresis for each topology during loading.

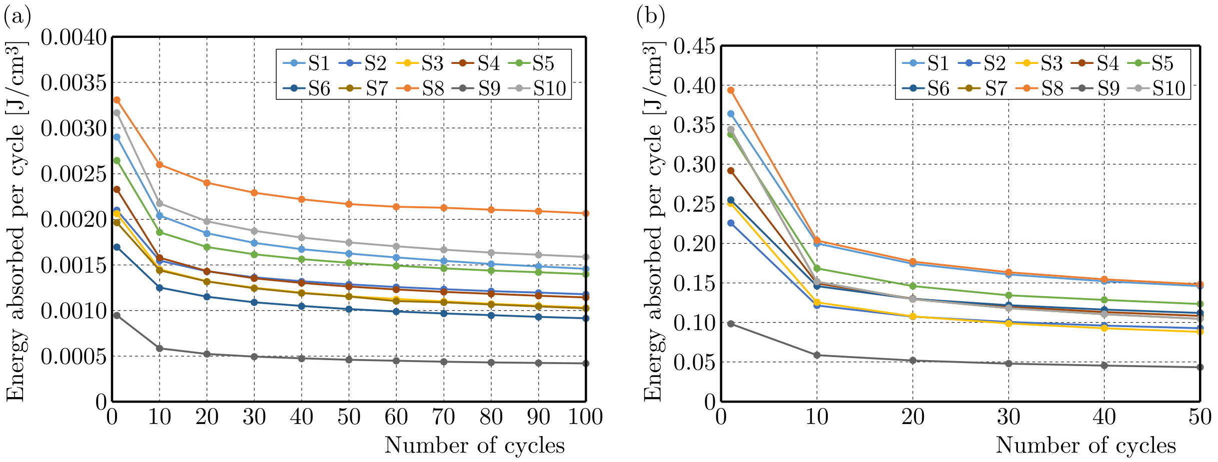

Fig. 4. Energy absorption variation during: (a) 100 cycles at 0.5 % strain; (b) 50 cycles at 5 % strain.

The second scenario presents the response of the samples over 50 cycles, up to a deformation of 1.5 mm (5 % strain), in order to capture the yielding and part of the plastic region.

To assess residual strain, two additional tests were conducted: one after one hour and one after 12 hours, to better understand the recovery behavior over time. Figure 5a displays the 1st (C1), the 50th (C50) cycle, and the two additional cycles for each sample. It can be noticed that the area of the hysteresis loop increases compared to the first scenario due to material loading in the plastic region, revealing higher plastic deformation. The decrease in force values with the number of performed cycles is also evident.

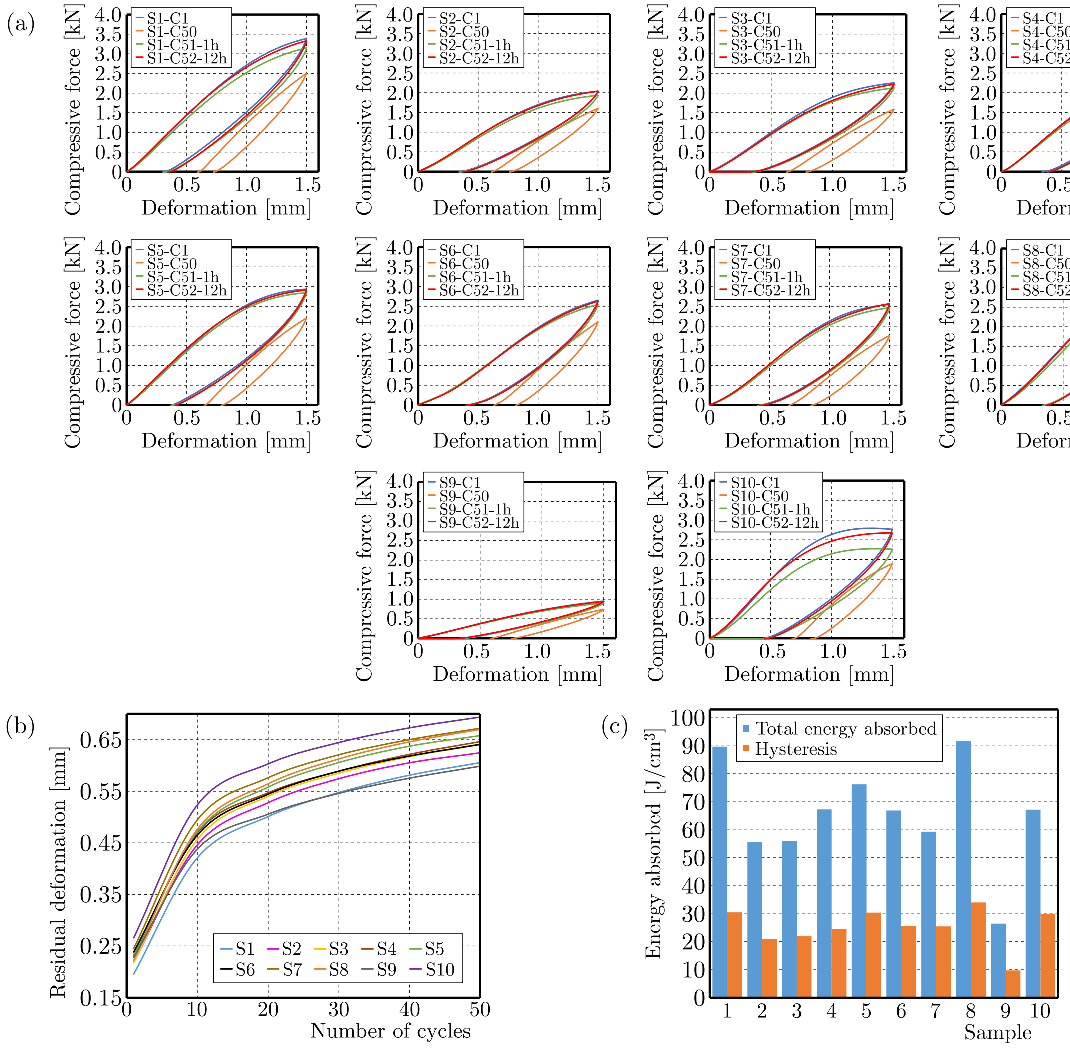

Fig. 5. (a) Cyclic compression results showing compressive force vs deformation plots for the 1st cycle (blue), the 50th cycle (orange) and two additional cycles after one hour of recovery time (green) and 12 h recovery time (red) for all topologies; (b) residual deformation accumulation during 50 cycles; (c) total energy absorbed and hysteresis for each sample during loading.

The green curve, representing the additional cycle performed after one hour (C51-1h), shows a lower compressive force, as the samples had not fully recovered to their initial shape. After 12 hours, however, most of the samples display similar evolutions to the first loading-unloading test, some even having slightly better performances. S6 demonstrates the smallest variation in performance among the 1st, the 51st (after 1 h), and the 52nd cycle (after 12 h) and the highest recovery rate, due to the geometry being architected from more cells of thinner walls that relax simultaneously. S10 exhibits the highest difference in recovery rates. A noticeable difference exists between the initial cycle and the force-deformation plot corresponding to the 51st cycle (C51-1h in Fig. 5). Even after 12 hours, the topology did not fully recover, given the fact that the red curve for the 52nd cycle (C52-12h) and the blue curve for the 1st cycle (C1) do not fully overlap. This shows that the continuous nature of the TPMS geometries provides better performances in terms of sample recovery and reusability.

Figure 5b shows that the stochastic geometry exhibits the highest value of residual deformation, followed by S7 and S8. Given the change of slope after the elastic region, most of the samples change their order compared to the first scenario. For example, the gyroid has a high level of residual deformation during the first scenario, but the rate at which it is accumulated decreases, so that during the second scenario it reaches the second-best position in terms of rigidity. However, this is not the case for S8, which accumulates strain with the fastest rate, changing from being the most rigid sample during the first scenario to the third-worst during the first 10 cycles of the second one.

Figure 5c displays the energy absorption capacity for each sample over 50 loading and unloading cycles, as well as the portion dissipated as hysteresis. It can be noticed that S8 maintains the best performance, while S10, which ranked second during the first scenario, dropped to the 5th place. This decline is attributed to the buckling of the struts, which causes premature softening and lower overall performance when more cycles are considered. Conversely, S6 exhibits improved performance, ranking 6th from the initial 9th position due to its lower residual strain accumulation. However, apart from S10 and S6, the ranking does not change, demonstrating the stability of the manufacturing process, material and topology response.

It can be noticed in Fig. 4b that the energy absorption capabilities exhibit a trend similar to that observed in the first scenario, where the damage behavior saturates after the first cycles. Here, however, the S10 sample does not rank so high, dropping from 3rd place to 6th place after the first 10 cycles. Also, S8 displays a steeper descending slope during the first 10 cycles, which coincides with the region where the sample accumulates the highest value of residual deformation. Beyond this region, the behavior stabilizes and the results are similar to the gyroid.

4. Conclusions

An implicit modeling approach was used to generate eight novel TPMS structures and one stochastic geometry, whose compressive behaviors were compared to the existing gyroid topology. Multiple samples were fabricated from a photo-polymeric resin, using an SLA technique.

Compressive testing revealed that topology S8 provided the best results in terms of yield strength and energy absorption capabilities, while displaying a deformation type very similar to the gyroid. Its yield strength values were up to 31 % higher than those of the gyroid, which ranked 3rd after the stochastic geometry. This topology, notated S10, demonstrated superior stiffness in the elastic deformation zone and approximately 6 % higher yield strength than the gyroid counterpart.

All the samples were tested following two scenarios: the first involved 100 cycles of loading and unloading up to 0.5 % strain at a speed of 1.5 mm/min, followed by one cycle after one hour of recovery. The second scenario consisted of 50 cycles at 5 % strain under the same loading speed, followed by two additional cycles after one hour and another after 12 hours of recovery. As expected, the hysteresis loops increased at higher strain values. During cyclic testing, these loops decreased in area, stabilizing at approximately 75 % of the loading force recorded during the first cycle. Topology S10 exhibited a different deformation mechanism due to the local buckling of the struts, which is also visible in the percentage of energy dissipated through hysteresis, only 44.4 % of the total energy being absorbed. In comparison, S8 registered a hysteresis dissipation percentage of 37 %, while the gyroid only 34.1 %.

From an energy absorption perspective, all the samples displayed a descendent trend that saturated after several cycles. Topology S8 showed the best results during both scenarios. However, the gyroid had a lower residual deformation at higher strain levels, leading to a more stable deformation over time, which improved the energy absorption capabilities when multiple cycles were considered. Overall, both S8 and the gyroid S1 displayed similar energy absorption capabilities after the first 10 cycles, when S8's behavior began to stabilize. The stochastic topology S10 demonstrated the second-best energy absorption capabilities for one-time compression or cyclic testing at low strain levels but ranked 6th during the second scenario due to the high residual strain and low recovery rate.

After the first 100 cycles at 0.5 % strain, the additional cycle performed after a recovery time of one hour showed a nearly identical behavior to the first loading cycle. The only outlier was the stochastic geometry which had a lower recovery rate than the TPMS specimens. Following the 50 cycles at 5 % strain, the samples recovered to approximately 95 % of the initial loading force after a one-hour recovery period and fully recovered after 12 hours. However, the stochastic topology recovered only 81 % of the initial loading force after one hour and 96 % after 12 hours.

Analyzing the results from all the cyclic tests performed, it was generally proven that TPMS topologies possess excellent loading-unloading repeatability, displaying a foam-type elastic behavior with a high recovery rate. Low cyclic compressive testing highlighted that the proposed TPMS topologies have a behavior showing high stability, and indicating their potential application as shock dampers and cushioning components.

Acknowledgments

Alexandru Vasile acknowledges the grant awarded by the Ministry of Education from Romania for completing his PhD studies under contract no. 06.87/05.10.2020.

References

1. Al-Ketan, O., Rowshan, R., Palazotto, A.N., & Abu Al-Rub, R.K. (2019). On mechanical properties of cellular steel solids with shell-like periodic architectures fabricated by selective laser sintering. *Journal of Engineering Materials and Technology*, *141*(2), Article 021009. https://doi.org/10.1115/1.4041874

2. Araya, M., Jaskari, M., Rautio, T., Guillén, T., & Järvenpää, A. (2024). Assessing the compressive and tensile properties of TPMS-Gyroid and stochastic Ti64 lattice structures: A study on laser powder bed fusion manufacturing for biomedical implants. *Journal of Science: Advanced Materials and Devices*, *9*(1), Article 100663. https://doi.org/10.1016/J.JSAMD.2023.100663

3. Cresswell, N.D., Ameri, A.A.H., Wang, J., Wang, H., Hazell, P., & Escobedo-Diaz, J.P. (2024). Characterization and modelling of triply periodic minimum surface (TPMS) lattice structures for energy absorption in automotive applications. In Z. Peng, *et al.* (Eds.), *Characterization of Minerals, Metals, and Materials 2024. TMS 2024. The Minerals, Metals & Materials Series* (pp. 295–305). Cham, Switzerland: Springer. https://doi.org/10.1007/978-3-031-50304-7_28

4. Feng, Y., Qiu, H., Gao, Y., Zheng, H., & Tan, J. (2020). Creative design for sandwich structures: A review. *International Journal of Advanced Robotic Systems*, *17*(3). https://doi.org/10.1177/1729881420921327

5. Gabrieli, R., Wenger, R., Mazza, M., Verné, E., & Baino, F. (2024). Design, stereolithographic 3D printing, and characterization of TPMS scaffolds. *Materials*, *17*(3), Article 654. https://doi.org/10.3390/MA17030654

6. Gao, T., Liu, K., Wang, X., Wei, K., & Wang, Z. (2024). Multi-level mechanism of biomimetic TPMS hybridizations with tailorable global homogeneity and heterogeneity. *Extreme Mechanics Letters*, *68*, Article 102136. https://doi.org/10.1016/J.EML.2024.102136

7. Lu, C., Hsieh, M., Huang, Z., Zhang, C., Lin, Y., Shen, Q., Chen, F., & Zhang, L. (2022). Architectural design and additive manufacturing of mechanical metamaterials: A review. *Engineering*, *17*, 44–63. https://doi.org/10.1016/J.ENG.2021.12.023

8. Novak, N., Borovinšek, M., Al-Ketan, O., Ren, Z., & Vesenjak, M. (2022). Impact and blast resistance of uniform and graded sandwich panels with TPMS cellular structures. *Composite Structures*, *300*, Article 116174. https://doi.org/10.1016/J.COMPSTRUCT.2022.116174

9. Ramírez, E.A., Béraud, N., Pourroy, F., Villeneuve, F., Amaya, J.L., & Museau, M. (2024). Design methodology of functionally graded cellular materials: Manipulating design parameters of triply periodic minimal surfaces through three-dimensional density distributions. *Computer-Aided Design*, *177*, Article 103778. https://doi.org/10.1016/J.CAD.2024.103778

10. Ronca, A., Rollo, G., Cerruti, P., Fei, G., Gan, X., Buonocore, G.G., Lavorgna, M., Xia, H., Silvestre, C., & Ambrosio, L. (2019). Selective laser sintering fabricated thermoplastic polyurethane/graphene cellular structures with tailorable properties and high strain sensitivity. *Applied Sciences*, *9*(5), Article 864. https://doi.org/10.3390/APP9050864

11. Schoen, A.H. (1970). Infinite periodic minimal surfaces without self-intersections. NASA Technical Note D-5541, Washington, D.C.: National Aeronautics and Space Administration.

12. Song, J., Wang, M., Li, D., & Zhang, J. (2024). Deformation and energy absorption performance of functionally graded TPMS structures fabricated by selective laser melting. *Applied Sciences*, *14*(5), Article 2064. https://doi.org/10.3390/APP14052064

13. Vasile, A., Constantinescu, D.M., Coropeţchi, I.C., Sorohan, Ş., & Apostol, D.A. (2024). Definition, fabrication, and compression testing of sandwich structures with novel TPMS-based cores. *Materials*, *17*(21), Article 5150. https://doi.org/10.3390/MA17215150

14. Viet, N.V., Waheed, W., Alazzam, A., & Zaki, W. (2023). Effective compressive behavior of functionally graded TPMS titanium implants with ingrown cortical or trabecular bone. *Composite Structures*, *303*, Article 116288. https://doi.org/10.1016/J.COMPSTRUCT.2022.116288

15. Wei, Y.P., Li, H.Q., Han, J.J., Ma, Y.C., Zhou, H.R., Cheng, J.C., Shi, J., Miao, Z.Q., Yu, B., & Lin, F. (2024). Mechanical and damping performances of TPMS lattice metamaterials fabricated by laser powder bed fusion. *China Foundry*, *21*(4), 327–333. https://doi.org/10.1007/S41230-024-4026-5

16. Yang, C., Wu, W., Fu, Z., & Zheng, H. (2023). Preparation and thermal insulation properties of TPMS 3Y-TZP ceramics using DLP 3D printing technology. *Journal of Material Science*, *58*(29), 11992–12007. https://doi.org/10.1007/S10853-023-08749-0

17. Yu, X., Zhou, J., Liang, H., Jiang, Z., & Wu, L. (2018). Mechanical metamaterials associated with stiffness, rigidity and compressibility: A brief review. *Progress in Materials Science*, *94*, 114–173. https://doi.org/10.1016/J.PMATSCI.2017.12.003

Manuscript received November 17, 2024; accepted for publication March 6, 2025;
published online June 28, 2025.